



Cite this: *RSC Adv.*, 2024, **14**, 17184

Molecular mechanism of elemental sulfur dissolution in H₂S under stratal conditions†

Sheng Yuan,^a Ying Wan,^b Li Wang,^b Nong Li,^b Mingli Yang,^b  ^a Shengping Yu^c and Li Zhang  ^{*a}

Resulting from the solubility reduction of elemental sulfur during the development of high sulfur gas formations, sulfur deposition often occurs to reduce the gas production and threaten the safety of gas wells. Understanding the dissolution mechanism of elemental sulfur in natural gas is essential to reduce the risk caused by sulfur deposition. Because of the harsh conditions in the high-sulfur formations, it remains challenging to *in situ* characterize the dissolution–precipitation processes, making deficient the knowledge of sulfur dissolution mechanism. The dissolution of sulfur allotropes (S_N, N = 2, 4, 6 and 8) in H₂S, the main solvent of sulfur in natural gas, is studied in this work by means of first-principles calculations and molecular dynamics simulations. While S₆ and S₈ undergo physical interaction with H₂S under the conditions corresponding to those at 1–6 km stratigraphic depths, S₂ and S₄ react with H₂S and form stable polysulfides. Unravelling the mechanism would be helpful for understanding and controlling the sulfur deposition in high-sulfur gas development.

Received 7th March 2024

Accepted 9th May 2024

DOI: 10.1039/d4ra01764a

rsc.li/rsc-advances

1. Introduction

The development of natural gas resources has become particularly important because of the increasing demand for clean energy around the world. Among the known natural gas reservoirs, those with a high-sulfur content account for a high proportion.^{1,2} High-sulfur gas reservoirs (HSGR) refer to reservoirs with a relatively high content (>2%) of hydrogen sulfide. In the HSGR development, sulfur deposition often occurs to block the pore throats that are abundant in the formations, remarkably lowering gas productivity.^{3–5} The occurrence of sulfur deposition comes from the solubility reduction of elemental sulfur in natural gas, which leads to the formation and precipitation of solid sulfur.^{3–7} Understanding the solubility evolution of elemental sulfur in natural gas is the basis of controlling sulfur deposition in practice.

Unfortunately, little is known about the molecular mechanism of sulfur dissolution in natural gas. For example, elemental sulfur has many allotropes, such as S_N (N = 2, 3, ..., 8), that may coexist under the formation conditions. Their contents vary with buried depth. S₂ content increases with

temperature, while S₈ content decreases with temperature.⁸ It remains unclear what the solute is among these allotropes, while H₂S has been well identified as the main solvent. Furthermore, there remains controversy whether the dissolution is a chemical or a physical process. It has been reported that elemental sulfur forms H₂S_n through association with H₂S under the temperature and pressure that are comparable to the formation conditions.^{8–11} Yu *et al.*¹¹ characterized the H₂S_N species at 120–250 °C in the S–H₂S–CH₄–H₂O systems with Raman spectroscopy. However, the number of S atoms in the polysulfides was not addressed in the experiments. Moreover, the *in situ* characterization of H₂S_N species in high-sulfur gas formation remains challenging. Polysulfides were not detected when the experimental temperature was below 373 K,⁹ but detected under 393–523 K.¹¹ In a computational study, He *et al.*¹² reported that in the ground-state S_N–H₂S complexes, the interaction between S_N (N = 2, 4, 6 and 8) and H₂S is as weak as a typical physical interaction, but the effect of temperature was not considered. Intermolecular physical interaction was assumed in some recent molecular simulations^{13–16} in which the force fields describing only the non-covalent interactions were used. In practice, however, the dissolution process is treated as a chemical reaction from which the Chrastil model¹⁷ is often used to estimate the solubility variations.^{18–23} It can be concluded that there is not sufficient evidence to classify the sulfur dissolution in natural gas as a chemical or a physical process.

The pronounced distinctions between chemical and physical processes may lead to different strategies in controlling the sulfur deposition in natural gas development. For example, the

^aInstitute of Atomic and Molecular Physics, Sichuan University, Chengdu 610065, China. E-mail: liizhang@scu.edu.cn

^bResearch Institute of Exploration and Development, PetroChina Southwest Oil and Gasfield Company, Chengdu 610213, China

^cKey Laboratory of General Chemistry of the National Ethnic Affairs Commission, School of Chemistry and Environment, Southwest Minzu University, Chengdu 610041, China

† Electronic supplementary information (ESI) available. See DOI: <https://doi.org/10.1039/d4ra01764a>



sensitivity with respect to temperature is usually different between these two processes because of their different energy barriers. Then, different temperature control strategies should be used for these two processes. It is therefore of great significance to identify the molecular mechanism of sulfur dissolution in natural gas. In this work, we first conducted first-principles molecular dynamics (FPMD) calculations on the S_N -H₂S mixtures of $N = 2, 4, 6$ and 8 , followed by quantum chemical calculations on their reaction paths and activation energies. Direct evidences are provided for the interaction between the solute and solvent molecules under a varying formation depth at which the temperature and pressure vary accordingly. Our study unravels the interaction mechanism of elementary sulfur with H₂S at the atomistic level, laying a basis for the further studies of real systems with additional components of CH₄, CO₂, etc.

2. Computational methods

S_N ($N = 2, 4, 6$ and 8) are selected as the solute molecules and H₂S as the solvent in our FPMD simulations. The ground-state structures of these allotropes have been well characterized in previous studies.^{24–26} Fig. 1 illustrates the molecular structures of sulfur oligomers. S₂ is a linear molecule with its two end atoms on the same side of the middle two atoms. S₆ and S₈ are cyclic with C_{3v} and C_{4v} symmetry, respectively. Given the low solubility of elemental sulfur in H₂S (about 0.001 in molar ratio), the computational models are constructed by putting randomly one hundred H₂S molecules and one S_N molecule into a cubic box with an initial density of 0.8 g cm⁻³. Periodic boundary conditions are applied in the three directions. Fig. 2 illustrates the models in which S₂–S₈ are surrounded by H₂S molecules. The side length of the cubic is about 1.95 nm, which is long enough to avoid from the interaction of two S_N molecules in the adjacent boxes.

The Born–Oppenheimer molecular dynamics (BOMD) simulations²⁷ are carried out under the isothermal-isobaric (NPT) ensemble. The temperature is controlled by using the canonical sampling through velocity rescaling (CSV) thermostat,²⁸ while the pressure is controlled using the Martyna–Tobias–Klein (MTK) barostat.²⁹ A number sets of temperature

and pressure are applied by considering the geological strata at Sichuan Basin in Southwest China, which is one of the main high-sulfur gas reservoirs in the world. Table 1 lists the pressure and temperature at different depths of the geological strata, which are used in our FPMD simulations. A total of 25 ps simulations are applied for all the systems. The simulations, unless otherwise mentioned, usually reach their equilibrations within 15 ps, while the remaining time is used for data collection and analysis. The time step is set to 1 fs. All atoms in the structures underwent unconstrained relaxation to their equilibrium positions without any fixation. Energy minimization was performed using the Orbital Transformation (OT) method, and the convergence criterion was set to 10^{-6} atomic units (a.u.). The exchange–correlation functional of Perdew–Burke–Ernzerhof (PBE)³⁰ with a semi-empirical DFT-D3 correction³¹ to the dispersion effect is used in the studied systems that are characterized by their weak intermolecular interaction. The double- ζ basis set (DZVP-MOLOPT)³² combined with Goedecker–Teter–Hutter (GTH) pseudopotentials³³ are employed in the DFT calculations. The energy cutoff is set to 400 Ry in the self-consistent calculations. The FPMD calculations are performed using the CP2K package's Quickstep module.^{34,35}

The radial distribution function (RDF), denoted as $g(r)$, stands as a frequently employed tool in statistical mechanics for characterizing the microstructure of disordered systems. The $g(r)$ signifies the probability of finding another particle (β) at a radial distance r , with any particle (α) acting as the center. It can be mathematically expressed by¹⁶

$$g(r) = \frac{n(r)}{4\pi r^2 \rho_0 \delta_r} \quad (1)$$

where r represents the specified central atomic radius. $n(r)$ denotes the number of particles of type β found within a shell of thickness δ_r . ρ_0 is the number density of particle of type β in the whole system. The RDF analysis, as implemented in the VMD software,³⁸ is applied to the coordinate files derived from FDMD simulations for the studied mixtures.

Then, the reaction paths and energy barriers for the reactions of S _{n} with H₂S are studied by DFT calculations with B3LYP^{39,40}/6-311++G(d,p)⁴¹ and M06-2X⁴²/6-311++G(2d,2p),⁴¹ as implemented in the Gaussian 16 package.⁴³ While B3LYP is known for its robust predictive power across a broad range of chemical systems, M06-2X provides enhanced accuracy particularly in systems involving complex non-covalent interactions. All the structures including reactants, intermediates, transition-state structures, and products are optimized and further verified with vibrational frequency calculations at the same level. The frequency scaling factor is 0.987 (ref. 44) under B3LYP/6-311++G(d,p), and 0.970 (ref. 45) under M06-2X/6-311++G(2d,2p). In these calculations, the long-range dispersion effect is considered by including the semi-empirical correction of DFT-D3.³¹ Since the FPMD simulations indicate that two H₂S molecules are involved in their reactions with S₂, the reaction paths with both one and two H₂S molecules are designed. The synchronous transit guided quasi-Newton (STQN) method^{46,47} is used to search for the transition-state structure based on the optimized structures, which are further identified by their exact

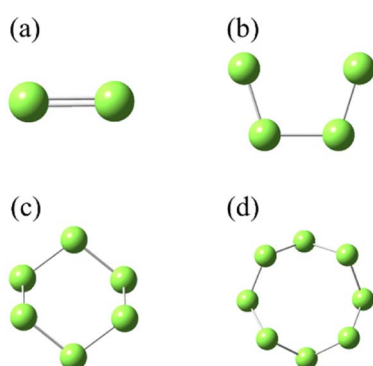


Fig. 1 The ground-state structures of molecular S₂ (a), S₄ (b), S₆ (c) and S₈ (d).



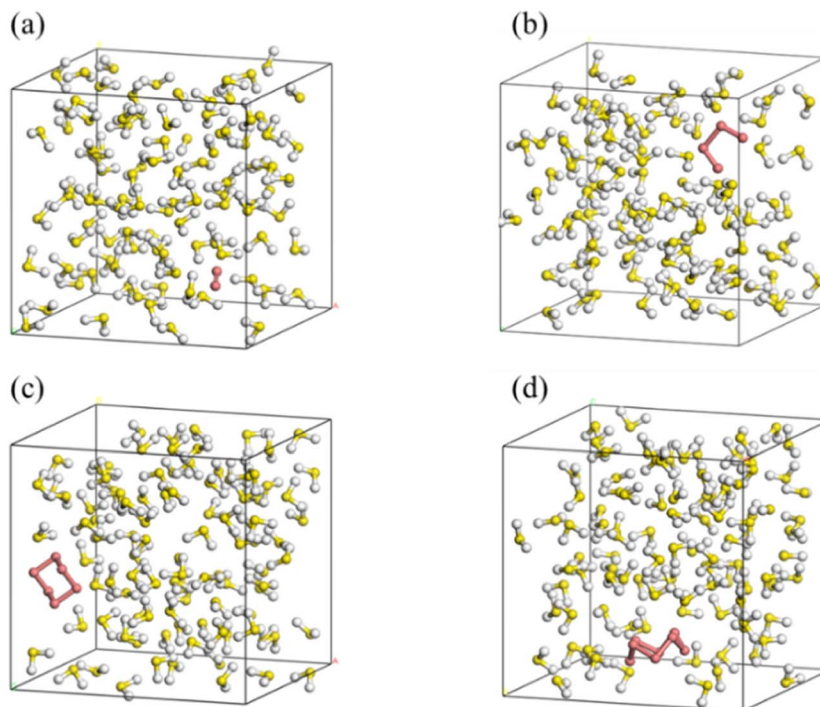


Fig. 2 Initial simulation models of S_2 (a), S_4 (b), S_6 (c) and S_8 (d) in H_2S (red for S_N and others for H_2S).

Table 1 Temperature and pressure at the depths of geological strata at Sichuan Basin, Southwest China.^{36,37}

Depth (km)	Pressure (MPa)	Temperature (K)
1	15	310
2	30	340
3	45	370
4	60	400
5	75	430
6	90	460

one imaginary frequency in vibrational spectra. The intrinsic reaction coordinate (IRC)^{34,48} calculations are performed to verify that the transition-state structures are able to connect contiguously the stable reactants, intermediates and products. The Shermo package⁴⁹ is used to derive the thermodynamic correction terms for the computed structures. Single-point calculations at the CCSD(T)⁵⁰ level with the aug-cc-pVQZ basis set⁵¹ are conducted for the optimized structures. The complete basis set (CBS) extrapolation⁵² is used to refine the computed values by conducting additional single-point calculations with the aug-cc-pVTZ basis set. The parameters for the CBS extrapolation are taken from the work by Neese *et al.*⁵³ Finally, the single-point energy is incorporated into the calculated free energy correction to yield the Gibbs free energy (ΔG).^{54,55}

3. Results and discussions

We first verify the validity of our computational strategy by comparing the computed density of pure H_2S with the

measurements.⁵⁶ Fig. 3 shows the predicted and measured densities of H_2S at a varying depth. The predicted values are the averaged densities obtained from the equilibrium configurations of H_2S relaxed in an NPT ensemble consisting of 100 H_2S molecules. The predicted densities overestimate the corresponding measurements by about 12–18%. The systematic overestimation in the predicted densities indicates the used functional and dispersion correction are inadequate to describe well the intermolecular interaction in the H_2S systems. The small size of the studied model may also have a contribution to the overestimation. The gaps remain almost unchanged between the predicted and measured values in the studied temperature and pressure ranges. It should be mentioned that

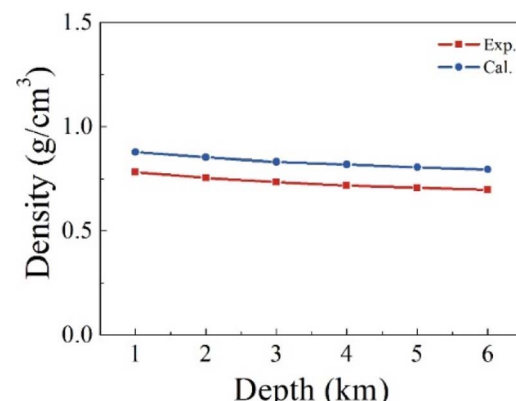


Fig. 3 Comparison between the computed and measured density of pure H_2S at a varying stratigraphic depth. The corresponding temperatures and pressures are given in Table 1.



the critical point is about 373 K and 9 MPa for H_2S ,⁵⁷ which is within the studied range. Nevertheless, our computations produce reliable density of pure H_2S , appropriate for the comparison of the reactivity of S_N allotropes with H_2S .

In their equilibrium configurations in the $\text{S}_2\text{--H}_2\text{S}$ mixtures, a new compound, H_2S_3 , is characterized in all the simulations at different stratigraphic depths. Fig. 4 shows the snapshots of the $\text{S}_2\text{--H}_2\text{S}$ mixtures after reaching their equilibrium states. At 1 km (Fig. 4a), H_2S_3 is a linear molecule totally different from the combination of H_2S and S_2 . Instead, the bonds in the system are reorganized. The three S atoms are in the middle, ended by two H atoms. The conformers of H_2S_3 are slightly different in the snapshots at different depths. However, it is evident that chemical reactions occur between H_2S and S_2 in all the cases.

The formation of H_2S_3 can be illustrated by tracking the interatomic bond lengths. By analyzing the molecular configuration variations in the slides, one finds that two H_2S molecules are involved in the chemical reactions. As presented in Fig. 5, the distances of three pairs, D1, D2 and D3, in H_2S_3 are thus defined for the involved molecules. At low temperature at 1 km, the slow rates allow us to have some details about the reaction. After 2 ps fluctuations, D1 drops to about 2.15 Å, and keeps steadily in the left time, indicating that the S atom of one H_2S molecule approaches to the S atom in S_2 and form a S–S bond. At about 15 ps, two S–H bonds are formed. One is formed by the other S atom in S_2 with the H atom in the second H_2S molecule.

The other is formed by the H atom in the first H_2S molecule with the S atom in the second H_2S molecule. It is in fact a reaction catalyzed by the second H_2S , which donates one H atom to S_2 and accept one H atom from the first H_2S .

Under higher temperatures at the deeper stratas, the reactions proceed in a similar path but a fast rate. For example, D1 is formed at about 5 ps at 3 km, while D2 and D3 at about 7 ps. At 5 and 6 km, the formation of the three bonds is completed within 1 ps. The averaged interatomic distances, D1, D2, and D3, in the equilibrium configurations are around 2.08, 1.37, and 1.36 Å, respectively. It is apparent that chemical bonds, one S–S and two S–H, are formed. The bond lengths are in agreement with previous studies^{58,59} in which the corresponding bond lengths are 2.054, 1.344, and 1.336 Å, respectively. Remember that temperature effect was not included in the previous studies.

The molecules of S_4 , S_6 , and S_8 have different experiences during the simulations. At all the studied stratigraphic depths, these three molecules do not show an evident reaction with H_2S . As presented in Fig. S1–S3 in the ESI,† the S_N molecule in the equilibrium configurations is surrounded by several H_2S molecules, but none of which forms a bond with S_N . In other words, only non-bonded interaction exists in the systems of H_2S and S_N ($N = 4, 6$ and 8). In the previous DFT calculations,¹² the interaction energy between H_2S and S_N ($N = 4, 6$, and 8) is about 1–3 kcal mol^{−1}, which indicates a typical physical interacting pattern between them. Under harsh conditions at the deepest

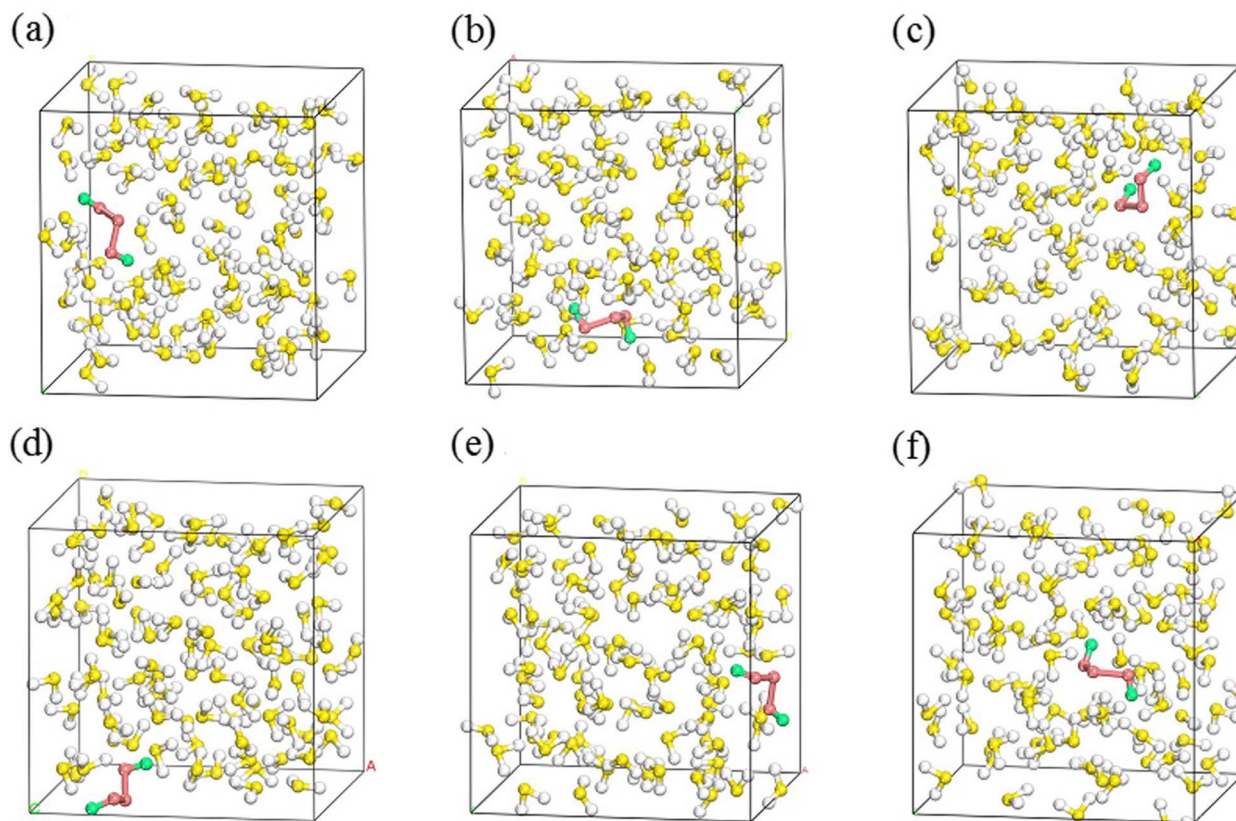


Fig. 4 Snapshots of the molecular configurations of S_N in H_2S at a varying stratigraphic depth (red and green balls are for S and H atoms in H_2S_3 , others for atoms in H_2S). 1 km (a), 2 km (b), 3 km (c), 4 km (d), 5 km (e) and 6 km (f).



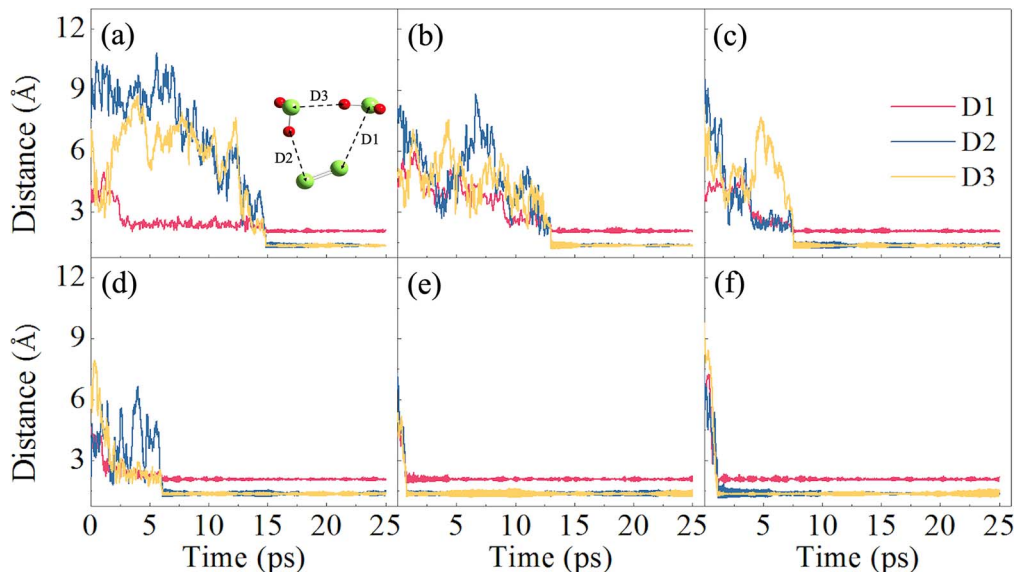


Fig. 5 Variations in the interatomic distances among the three molecules involved in the reactions of S_2 with H_2S . The involved atoms are traced from the last frame of the simulations. The interatomic distances, D1, D2 and D3, are marked in the insert (a) where S atoms are in green and hydrogen atoms in red. 1 km (a), 2 km (b), 3 km (c), 4 km (d), 5 km (e) and 6 km (f).

strata (460 K and 90 MPa), the three molecules retain their structures, as shown in Fig. S1–S3.[†]

Fig. 6 shows the RDF of the mixtures of S_N with H_2S . The interatomic distances between the S atom in S_N and H/S atom in H_2S are given. For S_4 , the first peaks occur at 3.95 Å for the intermolecular S–S (Fig. 6d), and 3.75 Å for intermolecular S–H (Fig. 6a). It is apparent that no chemical bonds are formed between S_4 and H_2S at all the studied stratigraphic depths. Similar analysis can be made for S_6 and S_8 (Fig. 6b, c, e and f), as well as a similar conclusion that S_6 and S_8 do not form chemical bonds with H_2S under the studied conditions. Moreover, the

peaks for the intermolecular S–S pairs are outstanding, while those for the S–H pairs are ignorable. This implies that the interaction is dominated by S–S pairs. It is the S atom in H_2S that interacts with S_N , which is similar to the case of S_2 with H_2S . The attraction of S–S pairs has also been addressed in other studies.¹⁶ The four atoms in S_4 may have different activity toward H_2S . Fig. S4[†] compares the RDFs of the central and the terminal atoms with the S atom in H_2S . The first peaks for these two types of atoms are similar both in position and height, and disordered H_2S distributions are noted at long distances,

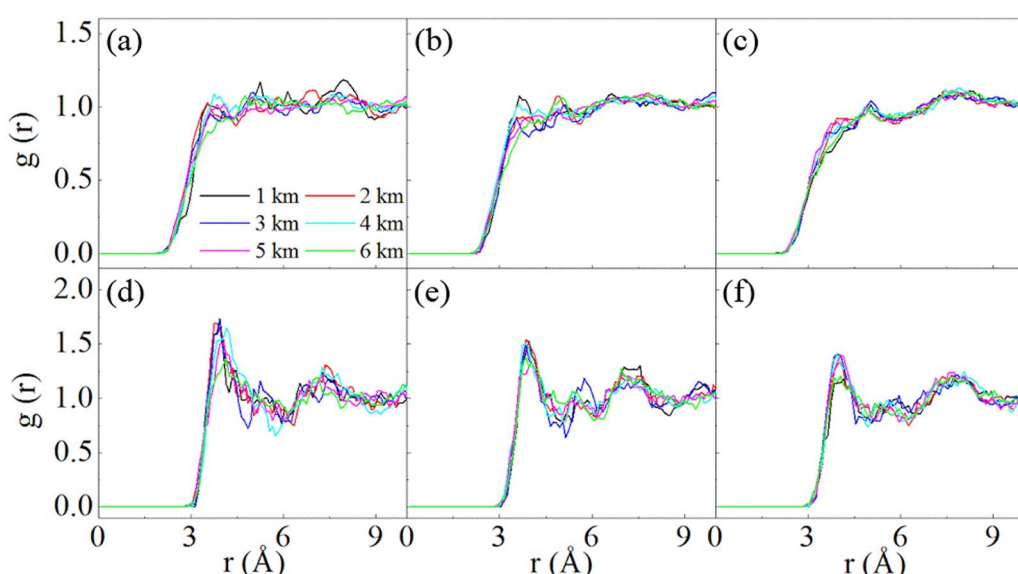


Fig. 6 RDFs of S atoms in S_N ($N = 2, 4, 8$) with atoms in H_2S at the stratigraphic depths of 1–6 km. S (S_4)–H (H_2S) (a), S (S_6)–H (H_2S) (b), S (S_8)–H (H_2S) (c), S (S_4)–S (H_2S) (d), S (S_6)–S (H_2S) (e) and S (S_8)–S (H_2S) (f).



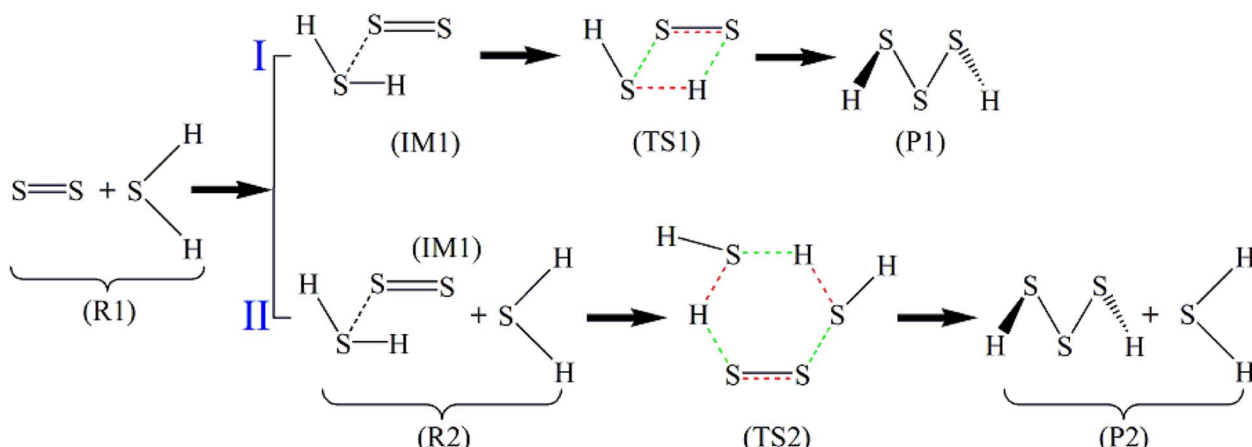
indicating that these two atoms do not exhibit much differences when they interact toward H_2S .

The dissolution of sulfur in H_2S thus has two paths, chemical and physical. In the physical path, S_N is surrounded by H_2S via weak non-bonded forces including Coulomb, van der Waals, dispersion, polarization, *etc.* The solubility contributed from physical interaction is determined by the strengths of these non-bonded forces. In the chemical path, the solubility is in fact contributed by the chemical reactions of S_N with H_2S . Understanding the reaction mechanism is thus helpful to control the solubility variations under the stratigraphic conditions. Although our AIMD simulations indicate that S_4 , S_6 , and S_8 do not react with H_2S . Considering the short simulation time, further investigations on their reaction paths and their activation barriers are necessary.

From the stoichiometric view, H_2S_3 is the combination of one H_2S molecule and one S_2 molecule, but the FPMD simulations indicate that two H_2S molecules sequentially interact with the S_2

molecule in the reactions. Therefore, two paths are designed for the reactions, which are presented in Scheme 1. In Path I, S_2 first binds with H_2S , forming an intermediate (IM1) in which only weak non-bonded interaction exists between them. A reorganization then occurs in IM1 to form a transition-state structure (TS1), followed by the formation of H_2S_3 (P1). In Path II, its first step, the formation of IM1, is the same with Path I. In the next step, IM1 interacts with the second H_2S . After the formation of a transition-state structure (TS2), H_2S_3 (P1) is formed, accompanied by the release of one H_2S molecule. Therefore, Path I contains two steps, while Path II has three steps.

All the structures shown in Scheme 1 are optimized and further identified with vibrational frequency calculations. Their structures are shown in Fig. 7 and their energy, and Gibbs free energy at 298 K and 0.1 MPa are given in Tables 2 and S1–S4.† Considering that the triplet state of S_2 is more stable by 16.98 kcal mol⁻¹ than its singlet, and the singlet state of H_2S_3 is more stable by 47.29 kcal mol⁻¹ than its triplet, both the singlet



Scheme 1 Reaction paths of S_2 with H_2S (the bonds to be broken are red, and those to be formed are in green).

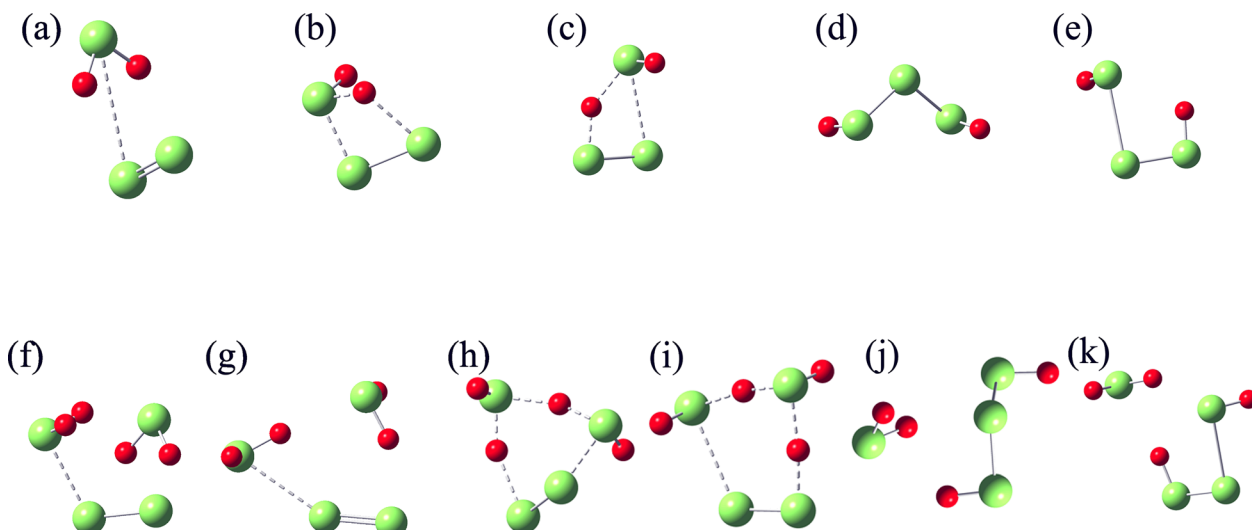


Fig. 7 Structure optimized at M06-2X/6-311+G(2d,2p) level. $\text{IM}1^T$ (a), $\text{TS}1^S$ (b), $\text{TS}1^T$ (c), $\text{P}1^S$ (d), $\text{P}1^T$ (e), $\text{R}2^S$ (f), $\text{R}2^T$ (g), $\text{TS}2^S$ (h), $\text{TS}2^T$ (i), $\text{P}2^S$ (j) and $\text{P}2^T$ (k). S and T denote the singlet and triplet states, respectively.



Table 2 Computed Gibbs free energy (ΔG , in kcal mol⁻¹) of reactants, intermediates, transition-state structures, and products (the Gibbs free energy of the triplet reactants in Paths I and II are taken as the references, and the values in parentheses are for the triplet states)

	R1	IM1	TS1	P1	R2	TS2	P2
B3LYP/6-311++G(d,p)	23.33 (0.00)	— (4.67)	45.70 (35.06)	-0.99 (32.71)	19.63 (0.00)	26.71 (31.89)	-7.22 (26.38)
CCSD(T)/aug-cc-pVQZ ^a	17.63 (0.00)	— (4.89)	55.39 (40.89)	-6.90 (36.48)	18.01 (0.00)	25.49 (41.58)	-13.40 (41.58)
CCSD(T)/aug-cc-pVTZ ^a	17.97 (0.00)	— (4.79)	56.19 (40.37)	-5.55 (36.14)	18.60 (0.00)	26.65 (41.51)	-11.95 (31.33)
M06-2X/6-311++G(2d,2p)	22.00 (0.00)	— (5.46)	37.69 (37.95)	-9.31 (34.15)	16.45 (0.00)	19.05 (32.13)	-17.10 (25.31)
CCSD(T)/aug-cc-pVQZ ^b	17.89 (0.00)	— (5.41)	37.07 (40.36)	-8.48 (36.29)	15.93 (0.00)	20.14 (36.54)	-16.40 (27.60)
CCSD(T)/aug-cc-pVTZ ^b	18.26 (0.00)	— (5.31)	38.73 (40.20)	-6.86 (36.10)	16.83 (0.00)	21.74 (36.54)	-14.78 (27.49)
CCSD(T)/CBS ^b	17.78 (0.00)	— (5.45)	36.59 (40.39)	-8.92 (36.38)	15.67 (0.00)	19.63 (36.48)	-16.87 (27.62)

^a On the B3LYP/6-311++G(d,p) optimized structures. ^b On the M06-2X/6-311++G(2d,2p) optimized structures.

and triplet states of these structures are taken into account in the structure optimization and vibrational frequency calculations. For IM1, only the triplet structure is identified, while its singlet structure is unstable.

Although structures optimized with B3LYP/6-311++G(d,p) and M06-2X/6-311++G(2d,2p) are topologically similar, they exhibit different stability at the CCSD(T) level at the CBS limit. As shown in Table 2, the ΔG values on the B3LYP-optimized structures are higher than those on the corresponding M06-2X-optimized structures. Therefore, the ΔG values obtained at the CCSD(T) level on the M06-2X structures are used for the subsequent analysis. Starting from IM1 in Path I, the H₂S molecule rotates about the intermolecular S···S linker until one of its H atoms bonds with the other S atom in S₂ to form TS1. TS1 has a four-membered ring in which the S-S double bond of S₂ is weakened, and becomes a single bond. Meanwhile, its two S atoms form one S-S bond and one S-H bond with H₂S, and one of the original S-H bonds is broken. P1 is then formed. Fig. 8 presents the energy landscape of Path I. The triplet structures are more stable for R1 and IM1, but less stable for TS1 and P1 than the corresponding singlet structures. A spin multiplicity transition from the triplet to the singlet states occurs in the formation of TS1. The identified energy barrier is

thus between the triplet IM1 and the singlet TS1, 31.66 kcal mol⁻¹, for Path I.

In Path II, starting from IM1, the second H₂S forms a six-membered ring with IM1 (TS2) with its S atom linking to the H atom of the first H₂S, and one of its H atoms linking to the S atom of S₂. An isodesmic reaction in which the type and number of the bonds formed in the product is identical to those broken in the reactant then occurs by losing two S-H bonds and simultaneously forming two S-H bonds. In the product, the formed H₂S is leaving from the H₂S₃. Similar to Path I, the singlet structures are more stable than the triplet structures for TS2 and P2. The energy barrier of Path II is thus between the triplet R2 and the singlet TS2, 20.14 kcal mol⁻¹. It is evident that Path II has a lower barrier than Path I, which is attributed to the stable six-membered ring structure and the isodesmic reorganization in TS. The isodesmic reactions usually proceed under facile conditions because the required energy for the bond breaking is mostly compensated by the released energy in the bond formation.⁶⁰⁻⁶² It is thus the reactions of S₂ with H₂S proceed by involving one S₂ and two H₂S molecules. In both paths, the products have lower energy than the corresponding reactants, indicating that the products are stable and the reactions are exothermic. The revealed kinetics verifies the

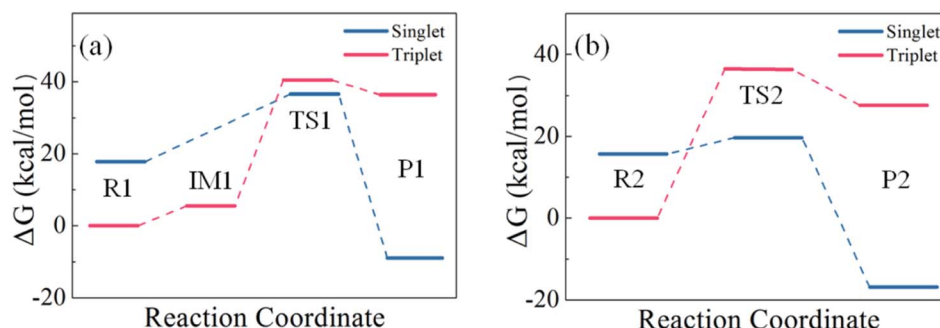


Fig. 8 Comparison of the energy barriers of the reactions of (a) one H₂S with one S₂ and (b) two H₂S with one S₂.



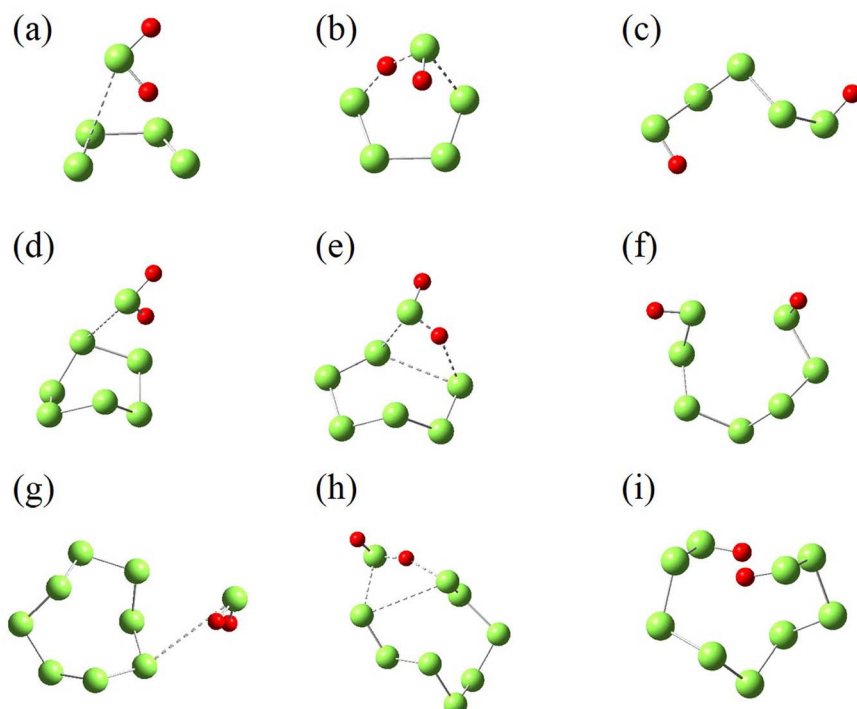


Fig. 9 Intermediates (IM3 (a), IM4 (d) and IM5 (g)), transition-state structures (TS3 (b), TS4 (e) and TS5 (h)), products (P3 (c), P4 (f) and P5 (i)) for the reactions of S_4 , S_6 and S_8 with H_2S , which are optimized at the M06-2X/6-311++G(2d,2p) level.

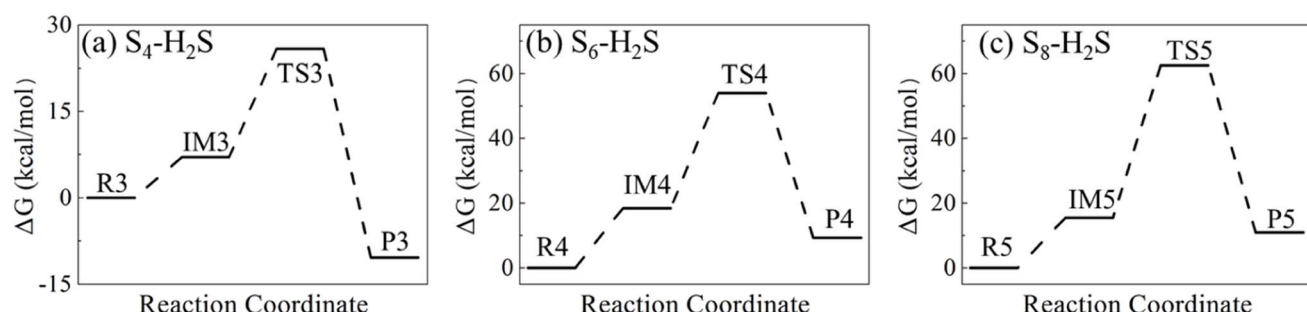


Fig. 10 Gibbs free energies of the reactants, intermediates, transition-state structures, and products for the reactions of S_4 (a), S_6 (b) and S_8 (c) with H_2S , which are calculated at the CCSD(T)/aug-cc-pVTZ level.

formation of H_2S_3 and the reaction mechanism observed in the FPMD simulations.

For $N = 4, 6$ and 8 , the reactions start from the attack of S atom in H_2S toward the terminal atom in S_4 , and one atom in S_6 and S_8 , forming the intermediates (IM3, IM4 and IM5 in Fig. 9). Then, one of H atoms in H_2S attacks the other terminal S atom in S_4 , forming the transition-state structure (TS3) with a six-membered ring. H_2S_5 is then formed by breaking the H-S bond in H_2S . For S_6 and S_8 , the transition-state structures (TS4 and TS5) have a four-membered ring consisting of two S atoms in S_N and one S and one H atom in H_2S . The formation of polysulfides, H_2S_7 and H_2S_9 , is facilitated by the breaking of S-S bond in S_N .

Fig. 10 illustrates the Gibbs free energies of the identified reactants, intermediates, transition-state structures and products shown in Fig. 9, and their optimized structures and thermodynamic parameters in Tables S12–S20 of ESI.† For the reaction of S_4 with H_2S , the energy barrier is 25.84 kcal mol⁻¹,

only 6.21 kcal mol⁻¹ higher than that of S_2 , indicating that S_4 is also reactive toward H_2S . The low barrier is attributed to the reactivity of the terminal S atoms in S_4 , as well as the stable six-membered ring in the transition-state structure. For S_6 and S_8 , the corresponding barriers are 54.02 and 62.54 kcal mol⁻¹, respectively. The high barriers are mainly attributed to the bond-breaking of S-S bond, and the strain in the four-membered rings in the transition-state structures. Therefore, S_6 and S_8 unlikely react with H_2S under typical geological conditions. The dissolution of S_N allotropes in H_2S has different mechanism, physical for S_6 and S_8 , and chemical for S_2 and S_4 .

4. Conclusions

DFT calculations and MD simulations are carried out to study the dissolution mechanism of elemental sulfur in its main solvent, H_2S , in high-sulfur gas formations. The interacting

models of sulfur allotropes S_N ($N = 2, 4, 6$ and 8) with H_2S molecules are created and simulated with FPMD under the temperature and pressure ranges corresponding the stratal depth of 1–6 km. While FPMD simulations indicate that only S_2 is active toward H_2S , quantum chemical calculations on the reaction paths reveal that both the reactions of S_2 and S_4 with H_2S have low activation energies, contrast to the high barriers in the reactions of S_6 and S_8 . These S_N allotropes have different activities toward H_2S , indicating a chemical dissolution for S_2 and S_4 in H_2S under typical geological conditions, and a physical dissolution for S_6 and S_8 . Our computations reveal the molecular mechanism of sulfur dissolution in H_2S , which lays the groundwork for future study of the solubility evolution of elemental sulfur in natural gas.

Author contributions

Sheng Yuan: conceptualization, data curation, writing original draft. Ying Wan: investigation, methodology, conceptualization. Li Wang: resources. Nong Li: validation, data curation. Mingli Yang: supervision, validation, Shengping Yu: data curation. Li Zhang: formal analysis, methodology, conceptualization.

Conflicts of interest

The authors declare no conflicts of interest.

Acknowledgements

This work was supported by the National Natural Science Foundation of China (No. 22173064) and Sichuan Kelite Oil & Gas Technology Service Co. Ltd.

References

- Y. Yang, L. Li, X. Wang, N. Qin, R. Zhang, Y. Zhao and Y. Tian, Simulation study of hydrogen sulfide removal in underground gas storage converted from the multilayered sour gas field, *Int. J. Coal Sci. Technol.*, 2023, **10**, 71.
- B. Fang, J. Hu, X. Wang and Y. Zhang, Transient analysis of horizontal wells with multiple fractures in sour gas reservoirs, *J. Nat. Gas Sci. Eng.*, 2022, **106**, 104730.
- X. Liu, S. Liu, Y. Wang, Y. Xiang, C. Qing, H. Zhang, H. Ren and C. Li, Estimation method of heterogeneous sulfur saturation distribution in high sulfur content gas reservoirs based on well test data, *Environ. Earth Sci.*, 2023, **82**, 115.
- X. Guo, P. Wang, J. Ma and C. Jia, Numerical simulation of sulfur deposition in wellbore of sour-gas reservoir, *Processes*, 2022, **10**, 1743.
- C. Zou, X. Wang, J. Hu, Y. Lv, B. Fang and Y. Zhang, A novel model for predicting the well production in high-sulfur-content gas reservoirs, *Geofluids*, 2021, **2021**, 6658711.
- X. Guo, P. Wang, J. Ma and T. Li, Experiment on gas-liquid sulfur relative permeability under high-temperature high-pressure sour gas reservoir condition, *Processes*, 2022, **10**, 2129.
- M. Shao, Q. Yang, B. Zhou, S. Dai, T. Li and F. Ahmad, Effect of sulfur deposition on the horizontal well inflow profile in the heterogeneous sulfur gas reservoir, *ACS Omega*, 2021, **6**, 5009–5018.
- R. A. Heidemann, A. V. Phoenix, K. Karan and L. A. Behie, A chemical equilibrium equation of state model for elemental sulfur and sulfur-containing fluids, *Ind. Eng. Chem. Res.*, 2001, **40**, 2160–2167.
- P. Cézac, J. P. Serin, J. Mercadier and G. Mouton, Modelling solubility of solid sulphur in natural gas, *Chem. Eng. J.*, 2007, **133**, 283–291.
- C. Li, G. Liu and Y. Peng, Solution mechanism of elemental sulfur in hydrogen sulfide under conditions of natural gas transmission, *Ind. Eng. Chem. Res.*, 2018, **58**, 440–447.
- Y. Yu, W. Hu, I.-M. Chou, L. Jiang, Y. Wan, Y. Li, Y. Xin and X. Wang, Species of sulfur in sour gas reservoir: Insights from *in situ* Raman spectroscopy of S - H_2S - CH_4 - H_2O system and its subsystems from 20 to 250 °C, *Geofluids*, 2021, **2021**, 6658711.
- L. He, L. Zhang, Y. Wan, N. Li and Y. Ren, Structures and energetics of elemental sulfur in hydrogen sulfide, *J. Cluster Sci.*, 2022, **33**, 1157–1164.
- X. Cui, W. Wang, M. Du, D. Ma and X. Zhang, Molecular simulation to explore the dissolution behavior of sulfur in carbon disulfide, *Molecules*, 2022, **27**, 4402.
- H. Chen, C. Liu and X. Xu, Molecular dynamic simulation of sulfur solubility in H_2S system, *Int. J. Mod. Phys. B*, 2019, **33**, 1950052.
- M. F. P. Mojdehi, M. G. Koli, M. D. O. Bolagh, M. G. Gardeh and S. M. Hashemianzadeh, A detailed computational study on binding of kinase inhibitors into β -cyclodextrin: Inclusion complex formation, *Mol. Syst. Des. Eng.*, 2021, **6**, 80–92.
- Y. Wei, L. Wang, Y. Yang, L. Wen, X. Huo, L. Zhang and M. Yang, Molecular mechanism in the solubility reduction of elemental sulfur in H_2S/CH_4 mixtures: A molecular modeling study, *Fluid Phase Equilib.*, 2023, **569**, 113764.
- J. Chrastil, Solubility of solids and liquids in supercritical gases, *J. Phys. Chem.*, 1982, **86**, 3016–3021.
- J. H. Hu, J. Z. Zhao, L. Wang, L. Y. Meng and Y. M. Li, Prediction model of elemental sulfur solubility in sour gas mixtures, *J. Nat. Gas Sci. Eng.*, 2014, **18**, 31–38.
- Q. Wang, X. Guo and R. Leng, In-depth study on the solubility of elemental sulfur in sour gas mixtures based on the Chrastil's association model, *Petroleum*, 2016, **2**, 425–434.
- G. Sodeifian, C. Garlapati, F. Razmimanesh and H. Nateghi, Solubility measurement and thermodynamic modeling of pantoprazole sodium sesquihydrate in supercritical carbon dioxide, *Sci. Rep.*, 2022, **12**, 7758.
- S. A. Sajadian, H. Peyrovedin, K. Zomorodian and M. Khorram, Using the supercritical carbon dioxide as the solvent of Nystatin: Studying the effect of co-solvent, experimental and correlating, *J. Supercrit. Fluids*, 2023, **194**, 105858.



22 G. Sodeifian, L. Nasri, F. Razmimanesh and M. A. Nooshabadi, Solubility of ibrutinib in supercritical carbon dioxide (Sc-CO₂): Data correlation and thermodynamic analysis, *J. Chem. Thermodyn.*, 2023, **182**, 107050.

23 X. Guo and Q. Wang, A new prediction model of elemental sulfur solubility in sour gas mixtures, *J. Nat. Gas Sci. Eng.*, 2016, **31**, 98–107.

24 M. Kumar and J. S. Francisco, Elemental sulfur aerosol-forming mechanism, *Proc. Natl. Acad. Sci. U. S. A.*, 2017, **114**, 864–869.

25 Y. Jin, G. Maroulis, X. Kuang, L. Ding, C. Lu, J. Wang, J. Lv, C. Zhang and M. Ju, Geometries, stabilities and fragmental channels of neutral and charged sulfur clusters: S_n^Q (n = 3–20, Q = 0, ±1), *Phys. Chem. Chem. Phys.*, 2015, **17**, 13590–13597.

26 R. Jones and P. Ballone, Density functional and Monte Carlo studies of sulfur. I. Structure and bonding in Sn rings and chains (n = 2–18), *J. Chem. Phys.*, 2003, **118**, 9257–9265.

27 V. Bakken, J. M. Millam and H. Bernhard Schlegel, *Ab initio* classical trajectories on the Born–Oppenheimer surface: Updating methods for Hessian-based integrators, *J. Chem. Phys.*, 1999, **111**, 8773–8777.

28 G. Bussi, D. Donadio and M. Parrinello, Canonical sampling through velocity rescaling, *J. Chem. Phys.*, 2007, **126**, 014101.

29 G. J. Martyna, D. J. Tobias and M. L. Klein, Constant pressure molecular dynamics algorithms, *J. Chem. Phys.*, 1994, **101**, 4177–4189.

30 J. P. Perdew, K. Burke and M. Ernzerhof, Generalized gradient approximation made simple, *Phys. Rev. Lett.*, 1996, **77**, 3865.

31 S. Grimme, J. Antony, S. Ehrlich and H. Krieg, A consistent and accurate *ab initio* parametrization of density functional dispersion correction (DFT-D) for the 94 elements H–Pu, *J. Chem. Phys.*, 2010, **132**, 15104.

32 J. Vande Vondel and J. Hutter, Gaussian basis sets for accurate calculations on molecular systems in gas and condensed phases, *J. Chem. Phys.*, 2007, **127**, 114105.

33 S. Goedecker, M. Teter and J. Hutter, Separable dual-space Gaussian pseudopotentials, *Phys. Rev. B: Condens. Matter Mater. Phys.*, 1996, **54**, 1703.

34 C. Gonzalez and H. B. Schlegel, An improved algorithm for reaction path following, *J. Chem. Phys.*, 1989, **90**, 2154–2161.

35 T. D. Kühne, M. Iannuzzi, M. Del Ben, V. V. Rybkin, P. Seewald, F. Stein, T. Laino, R. Z. Khaliullin, O. Schütt and F. Schiffmann, CP2K: An electronic structure and molecular dynamics software package-Quickstep: Efficient and accurate electronic structure calculations, *J. Chem. Phys.*, 2020, **152**, 194103.

36 K. Wang, B. Zhang and T. Kang, Effect of geological depths on CH₄ adsorption, diffusion, and swelling in kaolinite by molecular simulations, *Energy Fuels*, 2020, **34**, 1620–1626.

37 H. Wu, L. Wen, L. Zhang, D. Wang, N. Li and M. Yang, Gas adsorption capacity of type-II kerogen at a varying burial depth, *Energy Fuels*, 2022, **36**, 7472–7482.

38 W. Humphrey, A. Dalke and K. Schulten, VMD: visual molecular dynamics, *J. Mol. Graphics*, 1996, **14**, 33–38.

39 C. Lee, W. Yang and R. G. Parr, Development of the Colle–Salvetti correlation-energy formula into a functional of the electron density, *Phys. Rev. B: Condens. Matter Mater. Phys.*, 1988, **37**, 785–789.

40 A. D. Becke, Density-functional exchange-energy approximation with correct asymptotic behavior, *Phys. Rev. A*, 1988, **38**, 3098–3100.

41 M. J. Frisch, J. A. Pople and J. S. Binkley, Self-consistent molecular orbital methods 25. Supplementary functions for Gaussian basis sets, *J. Chem. Phys.*, 1984, **80**, 3265–3269.

42 Y. Zhao and D. G. Truhlar, The M06 suite of density functionals for main group thermochemistry, thermochemical kinetics, noncovalent interactions, excited states, and transition elements: two new functionals and systematic testing of four M06-class functionals and 12 other functionals, *Theor. Chem. Acc.*, 2008, **120**, 215–241.

43 M. J. Frisch, G. W. Trucks, H. B. Schlegel and *et al.*, *Gaussian 16, Revision B.01*, Gaussian, Inc., Wallingford, CT, 2016.

44 J. P. Merrick, D. Moran and L. Radom, An evaluation of harmonic vibrational frequency scale factors, *J. Phys. Chem. A*, 2007, **111**, 11683–11700.

45 I. Alecu, J. Zheng, Y. Zhao and D. G. Truhlar, Computational thermochemistry: scale factor databases and scale factors for vibrational frequencies obtained from electronic model chemistries, *J. Chem. Theory Comput.*, 2010, **6**, 2872–2887.

46 C. Peng and H. Bernhard Schlegel, Combining synchronous transit and quasi-newton methods to find transition states, *Isr. J. Chem.*, 1993, **33**, 449–454.

47 C. Peng, P. Y. Ayala, H. B. Schlegel and M. J. Frisch, Using redundant internal coordinates to optimize equilibrium geometries and transition states, *J. Comput. Chem.*, 1996, **17**, 49–56.

48 C. Gonzalez and H. B. Schlegel, Reaction path following in mass-weighted internal coordinates, *J. Phys. Chem.*, 1990, **94**, 5523–5527.

49 T. Lu and Q. Chen, Shermo: A general code for calculating molecular thermochemistry properties, *Comput. Theor. Chem.*, 2021, **1200**, 113249.

50 K. Raghavachari, G. W. Trucks, J. A. Pople and M. Head-Gordon, A fifth-order perturbation comparison of electron correlation theories, *Chem. Phys. Lett.*, 1989, **157**, 479–483.

51 D. E. Woon and T. H. Dunning Jr, Gaussian basis sets for use in correlated molecular calculations. III. The atoms aluminum through argon, *J. Chem. Phys.*, 1993, **98**, 1358–1371.

52 K. A. Peterson, D. E. Woon and T. H. Dunning Jr, Benchmark calculations with correlated molecular wave functions. IV. The classical barrier height of the H + H₂ → H² + H reaction, *J. Chem. Phys.*, 1994, **100**, 7410–7415.

53 F. Neese, A. Hansen and D. G. Liakos, Efficient and accurate approximations to the local coupled cluster singles doubles method using a truncated pair natural orbital basis, *J. Chem. Phys.*, 2009, **131**, 064103.

54 J. Luo, C. Cui, S. Sun, Z. Hu, R. Ma, M. Wang and J. Lin, Leveraging CO₂ to directionally control the H₂/CO ratio in continuous microwave pyrolysis/gasification of waste plastics: Quantitative analysis of CO₂ and density



functional theory calculations of regulation mechanism, *Chem. Eng. J.*, 2022, **435**, 134794.

55 S. Liu, L. Shan, G. Li, B. S. Underwood and C. Qi, Molecular-based asphalt oxidation reaction mechanism and aging resistance optimization strategies based on quantum chemistry, *Mater. Des.*, 2022, **223**, 111225.

56 N. Sakoda and M. Uematsu, A thermodynamic property model for fluid phase hydrogen sulfide, *Int. J. Thermophys.*, 2004, **25**, 709–737.

57 A. Cubitt, C. Henderson, L. Staveley, I. Fonseca, A. Ferreira and L. Lobo, Some thermodynamic properties of liquid hydrogen sulphide and deuterium sulphide, *J. Chem. Thermodyn.*, 1987, **19**, 703–710.

58 M. Liedtke, K. Yamada, G. Winnewisser and J. Hahn, Molecular structure of cis-and trans- H_2S_3 , *J. Mol. Struct.*, 1997, **413**, 265–270.

59 R. L. Cook, F. C. De Lucia and P. Helminger, Molecular force field and structure of hydrogen sulfide: recent microwave results, *J. Mol. Struct.*, 1975, **28**, 237–246.

60 W. J. Hehre, R. Ditchfield, L. Radom and J. A. Pople, Molecular orbital theory of the electronic structure of organic compounds. V. Molecular theory of bond separation, *J. Am. Chem. Soc.*, 1970, **92**, 4796–4801.

61 S. E. Wheeler, K. N. Houk, P. v. R. Schleyer and W. D. Allen, A hierarchy of homodesmotic reactions for thermochemistry, *J. Am. Chem. Soc.*, 2009, **131**, 2547–2560.

62 J. Xue, Y. S. Zhang, Z. Huan, J. D. Yang and J. P. Cheng, Deoxygenation of phosphine oxides by $\text{P}^{\text{III}}/\text{P}^{\text{V}} = \text{O}$ redox catalysis via successive isodesmic reactions, *J. Am. Chem. Soc.*, 2023, **145**, 15589–15599.

